J. Plasma Phys. (2024), *vol*. 90, 975900205
Published by Cambridge University Press
doi:10.1017/S0022377824000485

Temporally resolved measurement of a force induced by a pulsed water-fuelled magnetron sputtering source

Sota Shimizu[1] **and Kazunori Takahashi**[1,2,†]

[1]Department of Electrical Engineering, Tohoku University, Sendai 980-8579, Japan

[2]National Institute for Fusion Science, Toki 509-5292, Japan

(Received 18 September 2023; revised 24 March 2024; accepted 26 March 2024)

A high-speed solenoid-type pulsed valve is applied to a water-fuelled magnetron sputtering thruster, which can lead a compact and neutralizer-free electric propulsion device by generating a thrust due to the ejection of the sputtered target material, in order to minimize the size of the gas feeding system. The pulsed valve is opened for approximately 5 msec and the gaseous water is introduced into the source via a gas line connected to the source. A dc high voltage is firstly applied between the cathode and the anode; then the discharge is sustained for the period in which a gas pressure enough for the discharge is maintained and a change in the discharge mode is observed during the discharge pulse. To investigate the impact of the mode change on the thrust generation, a temporally resolved measurement of the force is equivalently performed by installing a pulsed voltage power supply and by changing the pulse width of the discharge voltage. The results show the temporal reduction of the thrust-to-power ratio during a pulsed discharge due to the nonlinear correlation between ion energy and sputtering yield. It is suggested that the use of a pulsed valve would be useful for downsizing of the electric propulsion system, while an optimization to properly control the gas flow rate is needed for further development.

Key words: magnetron sputtering, water plasma, electric propulsion

Nomenclature

z	axial position
k	calibration coefficient relating the amplitude of the target swing to impulse bit
I_{bit}	impulse bit induced by sputtered atoms
I_{bitcold}	impulse bit induced by cold gas supplying
t	time
$F(t)$	force induced by sputtered atoms
Y	sputtering yield
m_s	mass of sputtered atom
v_s	exhaust velocity of sputtered atom
A	cross-section of particle flow
$\dot{m}_s$	mass flow rate of sputtered atoms

† Email address for correspondence: kazunori.takahashi.e8@tohoku.ac.jp

I_d discharge current
I_i ion current
I_e electron current
P electric power to sustain a discharge
F/P thrust-to-power ratio
e elementary charge

Greek Symbols

δV the first swing of the target oscillation
Γ_s particle flux
γ secondary electron emission coefficient
ε ion energy impinging the target

1. Introduction

A magnetron sputtering source has been widely used for thin film deposition in the field of semiconductor manufacturing (Bräuer *et al.* 2010; Anders 2014; Greczynski *et al.* 2014). Typically, the magnetron sputtering source has a radial magnetic field near the cathode surface, and axial electric fields are formed by applying a discharge voltage between the cathode and the anode. The electrons in the plasma are efficiently confined due to the $\boldsymbol{E} \times \boldsymbol{B}$ drift motion ($\boldsymbol{E}$ and $\boldsymbol{B}$ are the electric and magnetic fields, respectively), resulting in an efficient high-density plasma production. The unmagnetized ions in the plasma are accelerated by the sheath voltage at the cathode surface and impinge on the target cathode. The target material is sputtered and ejected via momentum transfer processes in the target materials (Rizzo *et al.* 2000). This type of source has a good efficiency and a low cost with a simple structure and electrical circuits, while the plasma production and sputtering cannot be individually controlled (Gudmundsson 2020). Other types of sputtering reactors such as electron cyclotron resonance or helicon-type sputtering that can control the ion energy and target bias separably have also been developed (Kanno *et al.* 1996; Chabert *et al.* 2000; Muñoz-García *et al.* 2014; Takahashi *et al.* 2020). In those types of sources, an external magnetic field and a radiofrequency generator are required; the cost is more expensive and the system becomes complicated compared with the magnetron source.

The choices of working gas species and target materials are the important issues for proper operation of the sputtering reactor (Gudmundsson 2020). Argon is often used to sustain the magnetron discharge (Zhang *et al.* 2004; Marikkannan *et al.* 2015). The direct current magnetron sputtering (DCMS) is applicable to the deposition of only electrically conductive materials, e.g. metals such as copper, molybdenum, aluminium and so on (Gudmundsson 2020). Radiofrequency power generators in the range of MHz are often used for the discharge power source to sputter insulator targets (Anderson, Mayer & Wehner 1962; Davidse & Maissel 1966; Bartzsch *et al.* 2003; Nihei, Sasakawa & Okimura 2008). When using a pulsed voltage generator, a highly ionized plasma can be often formed, which is called high-power impulse magnetron sputtering (HiPIMS) (Sarakinos, Alami & Konstantinidis 2010; Antonin *et al.* 2014; Ghailane *et al.* 2020). It has been well known that the sputtering yield is also an important parameter, which is defined as the number of sputtered atoms by a single ion impinging on the target cathode, in addition to the discharge power. The sputtering yield depends on the ion species, the target species and the ion energy corresponding to the sheath voltage at the cathode surface (Doerner, Whyte & Goebel 2003; Gudmundsson 2020).

Andersson and Anders have proposed the application of the magnetron source to electric propulsion (EP) for spacecraft (Andersson & Anders 2008; Anders & Andersson 2013).

https://doi.org/10.1017/S0022377824000485 Published online by Cambridge University Press

One of the authors has demonstrated the thrust generation by an argon-fuelled DCMS. Since the neutral atoms sputtered from the cathode are responsible for the momentum ejection from the system, the DCMS seems to be applicable to a compact EP device having a single dc (direct current) power supply and no neutralizer. The subsequent experiment has shown that the thrust characteristic significantly depends on the discharge modes, where the thrusts imparted by the DCMS and the HiPIMS have been compared with Takahashi & Miura (2021*a*). It has been shown that the HiPIMS mode lowers the thrust-to-power ratio, which can be interpreted as a result of ionizations of the sputtered target atoms due to its high-density operation, where the ionized atoms are trapped by the electric field and do not contribute to the thrust generation. To operate these magnetron sources with argon, a high-pressure gas tank has to be mounted on satellites, which prevents the EP devices from being compact. Therefore, the authors have previously operated the DCMS with a water propellant that can be stored with no high-pressure gas storage tank, where the gaseous water flow rate is controlled by using a commercial mass flow controller having a size of approximately 81 mm in width, 28.6 mm in depth and 130 mm in height (Shimizu & Takahashi 2023). The results have demonstrated a thrust of 0.4 mN, specific impulse of 350 sec and thrust-to-power ratio of 4 mN kW^{-1}, which are comparable to the previously studied performance for the gridded ion thruster operated with H_2O (Ataka *et al.* 2021). However, the above-mentioned mass flow controller cannot be mounted in a unit of small CubeSat satellites due to their size restriction of $10 \times 10 \times 10$ cm. To further downsize the EP device utilizing the magnetron plasma production and the sputtering, the development of a compact gas feeding system is still a challenging issue in this type of EP device.

In the present study, a high-speed solenoid pulsed valve is utilized instead of the mass flow controller to downsize the gas feeding system, where the valve is mounted between the liquid water tank and the chamber. When the pressure at the water tank is reduced to the vaporized pressure of the water, gaseous water can exist between the liquid water and the valve. A small amount of gaseous water can be introduced into the magnetron source by pulsing the valve. The size of the pulsed valve is approximately 19 mm in width, 19 mm in depth and 55 mm in height, being much smaller than the mass flow controller, contributing to downsizing the EP device. The thrust-to-power ratio is assessed by measuring the impulse bit exerted on a target plate here. Since the thrust-to-power ratio is observed to be reduced for the pulsed valve operation, the temporally resolved measurement of the force imparted to the target plate is performed by alternating the dc voltage power supply to the pulsed one.

2. Experimental set-up

Figure 1 shows the schematic diagram of experimental set-up. Experiments are performed with the previously used magnetron sputtering source attached to the 260-mm-diameter and 732-mm-long cylindrical vacuum chamber evacuated by a turbomolecular pump to a base pressure less than 1 mPa, which is measured by an ionization gauge attached to the chamber sidewall. The annular inner and outer permanent magnets are installed behind the 45 mm-diameter cathode target made of copper, and provide a radial magnetic field of approximately 500 Gauss near the cathode surface (Shimizu & Takahashi 2023). The cathode is mounted on a ceramic insulator and a stainless-steel anode, which is further attached to the chamber via another ceramic insulator, as drawn in figure 1. This structure allows us to apply a high voltage of less than 1 kV by a voltage power supply electrically floating from the grounded chamber wall. Gaseous water is introduced from the eight small concentric holes made on the cathode. A high-speed solenoid pulsed valve having a response time of approximately

https://doi.org/10.1017/S0022377824000485 Published online by Cambridge University Press

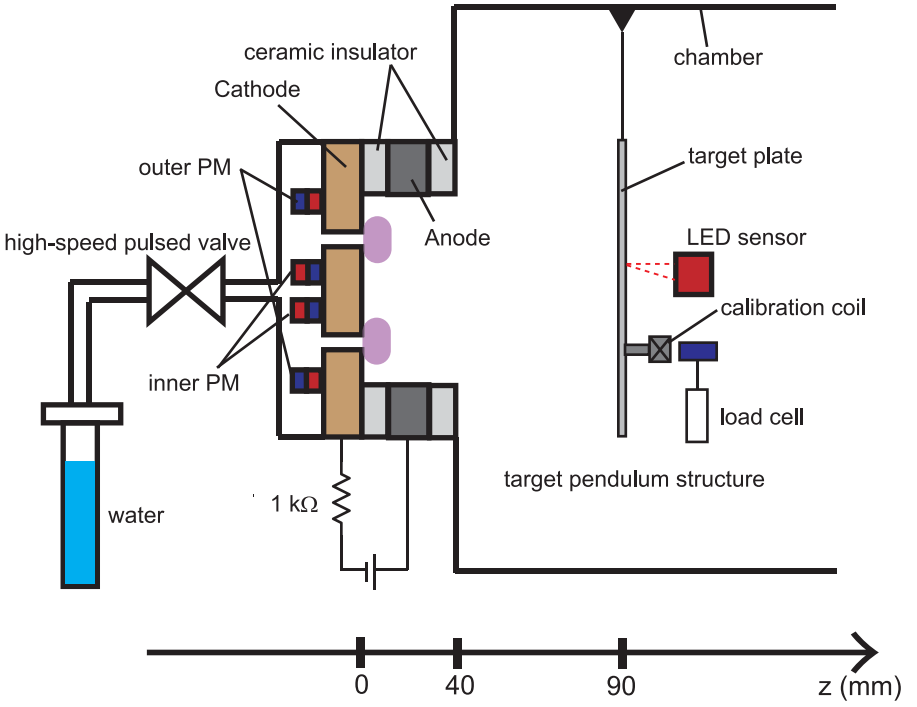

FIGURE 1. Schematic diagram of experimental set-up.

5 ms is inserted in series between the source and the liquid water tank, as drawn in figure 1. The liquid water is vaporized when the pressure between the pulsed valve and the water tank is less than the water vaporization pressure (∼3 kPa at the room temperature); the gaseous water can be introduced into the source by opening the pulsed valve. The mass flow introduced into the chamber is very roughly changed by the pulse width of the solenoid valve and two different pulse widths of 5 and 10 ms are tested here. It is noted that the temperatures of the source structure, the gas feeding pipes, the pulsed valve and the water tank are maintained at 40 °C to prevent the water from being iced and to minimize the change in the vaporization pressure. Prior to opening the pulsed valve, a dc voltage is applied between the anode and cathode through the resistor of 1 kΩ, where the dc power supply is electrically isolated from the surroundings by an isolation transformer, which ensures that net current flowing into the grounded chamber is zero. When turning on the pulsed valve, a transient formation of a donut-shape plasma can be visually seen from the glass view ports at the chamber wall.

Impulse bit or thrust imparted by the sputtering resulting from the plasma production is assessed using a pendulum target balance Very briefly, a target pendulum structure mounted on a pivot is installed downstream of the magnetron source at $z = 10$ cm and its displacement induced by an axial force is measured by a lightning electric diode (LED) displacement sensor located further downstream of the target. Before pumping down the chamber, a calibration coefficient relating the amplitude of the first swing to the impulse bit is obtained, and the detailed procedure can be found in Takahashi, Komuro & Ando (2015). The calibration result plotted by open squares in figure 2 can be well fitted by a linear line and gives the calibration coefficient of $k = I_{\mathrm{bit}}/\delta V \sim 1.8$. In the experiments, the impulse bits exerted by the gaseous water, the plasma and the sputtered atoms are included in the measurement. Therefore, the impulse bit $I_{\mathrm{bit\,cold}}$ induced only by the gaseous

https://doi.org/10.1017/S0022377824000485 Published online by Cambridge University Press

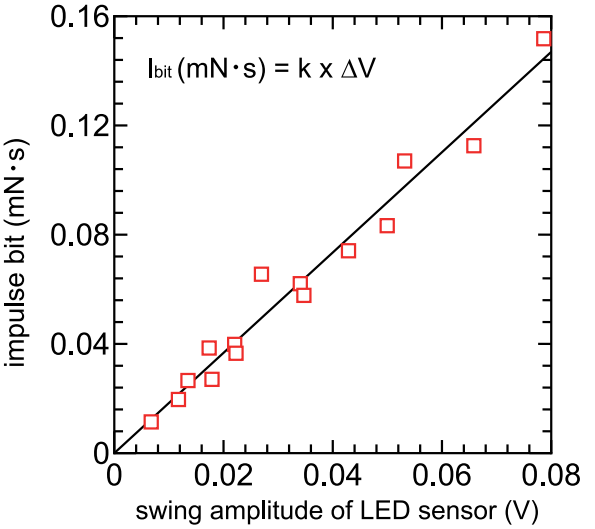

FIGURE 2. Measured swing amplitude of the LED sensor (open squares) as a function of the known impulse bit, together with a fitted linear line (a black solid line) giving the calibration coefficient of $k = 1.8$ (mN · s) V^{-1}.

water is measured in advance with no discharge voltage. The impulse bit exerted by the plasma production is obtained by subtracting $I_{\text{bit cold}}$ from the measurement.

As described later in the § 3 (Experimental results), a change in the discharge mode is detected during the discharge pulse when introducing the gaseous water by using the pulsed valve. In order to discuss the temporal variation of the force, the impulse bit induced by the controlled pulsed discharge voltage is measured for various pulse width of the discharge voltage. The impulse bit I_{bit12} by the force $F(t)$ between the times of t_1 and t_2 is generally given by

$$I_{\text{bit12}} = \int_{t_1}^{t_2} F(t)\,\mathrm{d}t = \int_{t_0}^{t_2} F(t)\,\mathrm{d}t - \int_{t_0}^{t_1} F(t)\,\mathrm{d}t, \tag{2.1}$$

where t_0 is defined as the time triggering the discharge. The first and second terms of ((2.1)) can be experimentally obtained by changing the pulse width of the discharge, which can be performed by the pulsed voltage power supply (Takahashi & Miura 2021*a*). In the present experiment, the voltage applied to the cathode through a 1 kΩ resistor is turned on at 10 msec after turning on the pulsed valve at $t = 0$ and the impulse bit is measured as a function of the turning-off time (t_1 and t_2); then, the force between t_1 and t_2 can be calculated as

$$F(t) = \frac{I_{\text{bit12}}}{t_2 t_1}. \tag{2.2}$$

3. Experimental results and discussion

3.1. *Discharge characteristics and impulse bit assessment*

Here, the discharge characteristics and the impulse bit are assessed in the operation with the pulsed gaseous water injection and the dc voltage power supply. Figure 3 shows the typical temporal evolutions of the voltage between the anode and the cathode (a red solid line) and the discharge current (a blue solid line), where the discharge voltage and the

https://doi.org/10.1017/S0022377824000485 Published online by Cambridge University Press

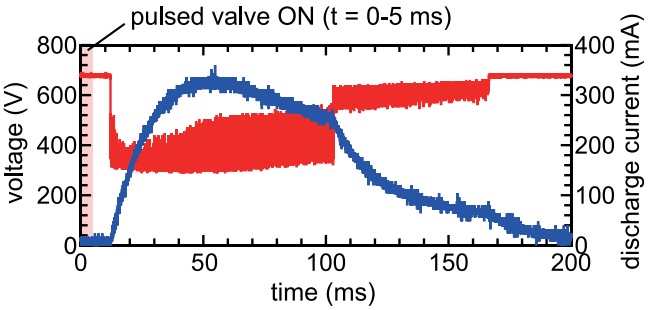

FIGURE 3. Typical temporal evolutions of the voltage between the anode and the cathode (a red solid line) and the discharge current (a blue solid line), where the output voltage of the dc power supply voltage is set at 700 V. It is noted that the pulsed valve is turned on for $t = 0$–5 ms, as shown by a red rectangle.

pulse width for opening the pulsed valve are set at 700 V and 5 ms, respectively. It is noted that the pulsed valve is opened at $t = 0$, as shown by a red rectangle in figure 3. Due to the voltage drop across the 1 kΩ resistor by the discharge current, the voltage between the anode and the cathode is reduced simultaneously with the discharge, where the discharge starts to occur at $t = 10$ ms, as can be seen in figure 3. It should be noted that the delay depends on the length of the gas injection line between the valve and the plasma source. The discharge is found to be sustained for approximately 160 ms in figure 3. For $t \sim 10$–100 msec, a relatively low-voltage and large-current mode is found to be sustained; then, the discharge mode is changed into a high-voltage and small-current mode. This type of mode change has been reported earlier (Morel *et al.* 2023); it seems to be caused by the temporal changes in the gas flow rate from the cathode holes and the pressure near the cathode surface. The energy consumed for the discharge can be calculated by temporally integrating the product of the measured voltage and current, being typically in the range of 30–100 J and depends on the voltage from the power supply and the pulse width of the valve.

Figure 4 shows the impulse bit measured by the target technique as a function of the discharge energy. The energy is changed by the dc voltage in the range of 650–830 V and the two different pulse widths of 5 and 10 ms for opening the valve are also tested, as plotted by the red filled circles and open squares, respectively. It should be emphasized again that the impulse bit exerted by the cold gas is eliminated in figure 4. For comparison, the measured thrusts as functions of the power for the continuous gas flow rates of 8 sccm and 10 sccm are plotted by blue open circles and filled squares, respectively, which had already reported in Shimizu & Takahashi (2023). The dashed lines in figure 4 show the thrust-to-power ratio, which is equivalent to the impulse bit divided by the energy for the pulsed operation mode. It is found that both the impulse bit and the thrust are proportional to the input energy and power, respectively. The present measurements plotted by the red symbols are in the range of 1–2 mN kW^{-1}, being half of the previously measured thrust-to-power ratio of 3–4 mN kW^{-1}. The operation with the pulsed valve has a significant advantage in terms of the size, as described already, while the reduction of the thrust-to-power ratio has to be understood, which will be useful for further development. Therefore, the temporally resolved measurement of the force is performed, as in the next section.

https://doi.org/10.1017/S0022377824000485 Published online by Cambridge University Press

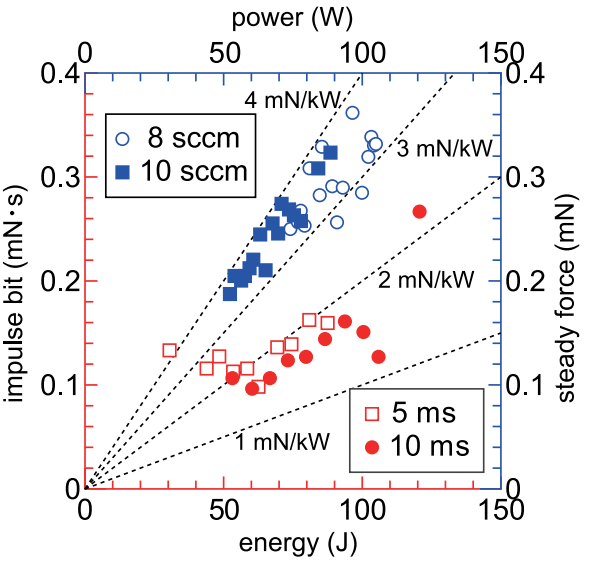

FIGURE 4. Measured impulse bit as a function of an input electric energy for the high-speed pulsed valve operation with the pulse widthsof 5 ms (red open squares) and 10 ms (red filled circles), together with dashed lines corresponding to the thrust-to-power ratios as labelled in the figure. The thrusts measured for the continuous gas feedings of 8 sccm (open circles) and 10 sccm (filled squares) by using the mass flow controller are plotted for comparison (Shimizu & Takahashi 2023).

3.2. *Temporally resolved force measurement*

The temporally resolved force measurement is conducted by using the pulsed voltage power supply, as described in § 2. Here, the power supply is turned on at $t = 10$ ms for all the conditions; while the turning-off time is changed to control the discharge duration time from 20 to 210 ms. Figure 5 shows the temporal evolutions of the voltage between the anode and the cathode (red solid lines) and the discharge current (blue solid lines) for the representative turning-off times of (*a*) 70 ms, (*b*) 120 ms and (*c*) 170 ms, where the pulsed voltage is turned on for the temporal region coloured red. It can be found that the temporal evolution before turning off the pulsed voltage is fairly unchanged; this fact validates the measurement of the temporal evolution of the force described in § 2. The typical error in the time of the discharge trigger is ± 5 ms and is small enough to estimate the temporal evolution of the force. Figure 6 shows the measured impulse bit as a function of the turning-off time, clearly showing the increase in the impulse bit with an increase in the turning-off time, i.e. an increase in the pulse width. It can be seen that the slope is clearly changed at a turning-off time above 100 ms, which is very close to the time of the discharge mode change. Figure 7 shows the estimated temporal evolutions of (*a*) the discharge power, (*b*) the force estimated from the data in figure 6 and (2.1) and (2.2) and (*c*) the thrust-to-power ratio calculated from figures 7(*a*) and 7(*b*). It is noted that a moving average is used to minimize the digital noise in the differential procedure in (2.2). The discharge power slightly decays, as seen in figure 7(*a*), while the force more conspicuously decays from ~ 0.4 to ~ 0.1 mN, as in figure 7(*b*). Therefore, the thrust-to-power ratio is found to decay significantly, as plotted in figure 7(*c*). The reduction of the thrust-to-power ratio for the high-voltage mode can be qualitatively interpreted by taking the sputtering yield Y into account as follows.

https://doi.org/10.1017/S0022377824000485 Published online by Cambridge University Press

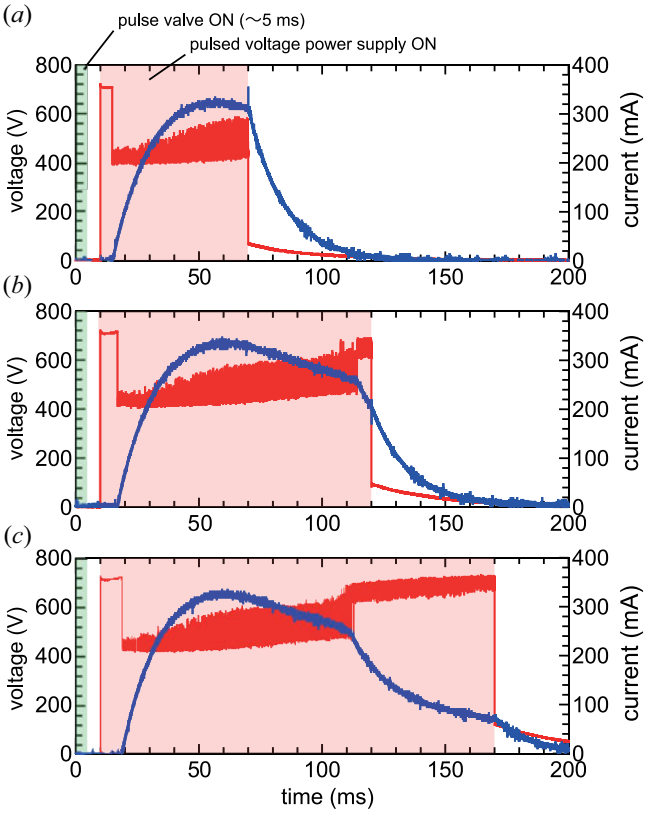

FIGURE 5. Temporal evolutions of the voltage between the anode and the cathode (red solid lines) and the discharge current (blue solid lines) for the representative turning-off times of (*a*) 70 ms, (*b*) 120 ms and (*c*) 170 ms, where the pulsed gas valve and the pulsed voltage are turned on for the temporal region coloured by green and red, respectively.

The force exerted by the ejected sputtered atoms can be briefly described by (Takahashi & Miura 2021*b*)

$$F = m_s v_s \Gamma_s A = \dot{m}_s v_s, \tag{3.1}$$

where F, m_s, v_s, Γ_s, A and $\dot{m}_s$, are the thrust, the mass of the sputtered atom, the exhaust velocity, the particle flux, the cross-section of the flow and the mass flow rate of sputtered atoms. The discharge current I_d is the sum of the ion current I_i and the secondary electron current $I_e = \gamma I_i$ as given by

$$I_d = I_i + I_e = (1 + \gamma) I_i, \tag{3.2}$$

where γ is the secondary electron emission coefficient. Since the mass flow rate of the sputtered atoms is proportional to the sputtering yield Y and the ion current, i.e. $\dot{m}_s \propto Y I_i$, the thrust-to-power ratio F/P is written as

$$F/P = \frac{\dot{m}_s v_s}{V_d I_d} \propto \frac{Y I_i v_s}{V_d I_d} = \frac{Y v_s}{(1 + \gamma) V_d}. \tag{3.3}$$

It is well known that the sputtering yield depends on the impinging energy ε of the ions, which is determined by the sheath voltage at the cathode surface and very

https://doi.org/10.1017/S0022377824000485 Published online by Cambridge University Press

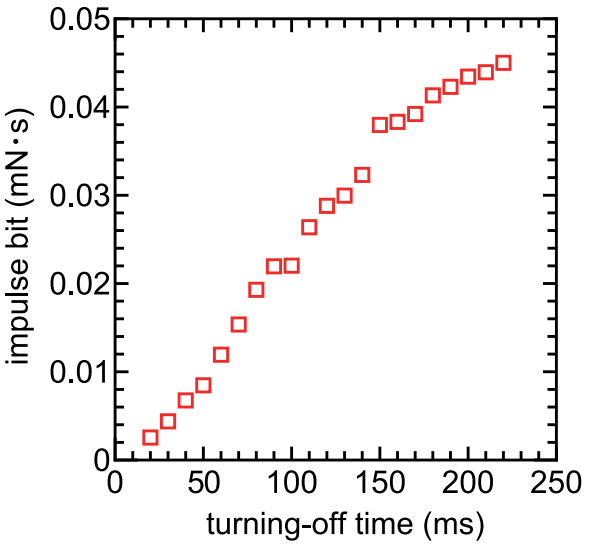

FIGURE 6. The measured impulse bit as a function of the turning-off time of the pulsed voltage.

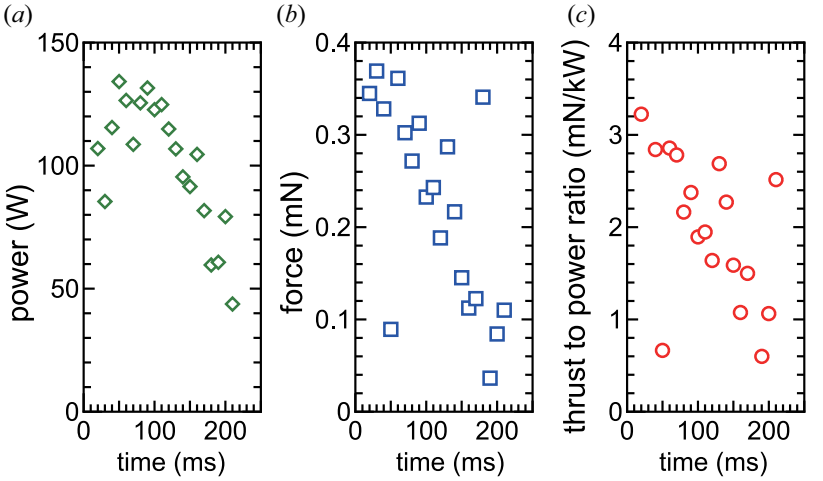

FIGURE 7. The estimated temporal evolutions of (*a*) the discharge power, (*b*) the force and (*c*) the thrust-to-power ratio, where the force is calculated according to (2.2).

close to the discharge voltage, i.e. $\varepsilon \sim eV_d$. Previous experiments and simulations have shown that the sputtering yield Y does not linearly increase with an increase in the ion energy ε, i.e. the ratio of $Y/\varepsilon \sim Y/eV_d$ decreases in the energy range of $\varepsilon > 600$ eV; see Mahne, Čekada & Panjan (2022), Schelfhout, Strijckmans & Depla (2020), Greene (2017), Somogyvári *et al.* (2012) and Anders (2010). Therefore, the thrust-to-power ratio F/P given by (3.1) is found to be reduced for the high-voltage and low-current mode. It is found that the thrust-to-power ratio for the low-voltage and high-current region at $t < 100$ ms is approximately 3 mN kW^{-1} and is very close to that obtained with the mass flow controller operation (see the blue open circles and filled squares in figure 4), validating the temporally resolved measurement of the force. The reduction of the thrust-to-power ratio for the

https://doi.org/10.1017/S0022377824000485 Published online by Cambridge University Press

high-voltage mode at $t > 100$ ms in figure 7(c) can be well explained by considering the change in the sputtering yield, as described by (3.3). The high-voltage and low-current discharge mode would result from the absence of gas; more stable controls of the gas flow and the pressure near the target cathode are required to improve the thruster performance.

4. Conclusions

The gaseous water is introduced into the magnetron sputtering source by using a high-speed solenoid pulsed valve toward a development of a compact EP device, where the thrust is generated by ejecting neutral target atoms. The impulse bit exerted on the pendulum target located downstream of the source is measured. The thrust-to-power ratio for the pulsed valve operation is smaller than that for the operation with the mass flow controller. The temporally resolved measurement of the force reveals that the high-voltage and low-current mode discharge results in lowering the thrust-to-power ratio due to the reduction of the ratio of the sputtering yield to the impinging energy of the ions. Availability of the pulsed valve for a compact gaseous water injection system is demonstrated here, while the optimized design of the gas feeding system for stable operation of the low-voltage and high-current mode still remains a further challenging issue.

Acknowledgements

Editor Cary Forest thanks the referees for their advice in evaluating this article.

Funding

This work is partially supported by Grant-in-Aid for Scientific Research (Grant Nos. 21K18611 and 23H05442) from the Japan Society for the Promotion of Science and Fusion Oriented REsearch for disruptive Science and Technology (FOREST) from Japan Science and Technology Agency (Grant No. JPMJFR212A).

Declaration of interest

The authors report no conflict of interest.

Data availability statement

The data that support the findings of this study are available from the corresponding author upon reasonable request.

Author contributions

S.S. and K.T. designed the concept of the experiment. The gas feeding system and the pulsed power supply were constructed by S.S. and K.T., respectively. The data were taken and analysed by S.S. and all authors contributed to interpreting the results. The manuscript written by S.S. was reviewed and edited by K.T.

REFERENCES

ANDERS, A. 2010 Deposition rates of high power impulse magnetron sputtering: physics and economics. *J. Vac. Sci. Technol.* A **28** (4), 783–790.

ANDERS, A. 2014 A review comparing cathodic arcs and high power impulse magnetron sputtering (HiPIMS). *Surf. Coat. Technol.* **257**, 308–325, 25 years of TiAlN hard coatings in research and industry.

ANDERS, A. & ANDERSSON, J. 2013 Very low pressure high power impulse triggered magnetron sputtering. US Patent 8,568,572.

ANDERSON, G.S., MAYER, W.N. & WEHNER, G.K. 1962 Sputtering of dielectrics by high-frequency fields. *J. Appl. Phys*. **33** (10), 2991–2992.

ANDERSSON, J. & ANDERS, A. 2008 Gasless sputtering: opportunities for ultraclean metallization, coatings in space, and propulsion. *Appl. Phys. Lett*. **92** (22), 221503.

ANTONIN, O., TIRON, V., COSTIN, C., POPA, G. & MINEA, T.M. 2014 On the HiPIMS benefits of multi-pulse operating mode. *J. Phys.* D*: Appl. Phys*. **48** (1), 015202.

ATAKA, Y., NAKAGAWA, Y., KOIZUMI, H. & KOMURASAKI, K. 2021 Improving the performance of a water ion thruster using biased electrodes. *Acta Astronaut*. **187**, 133–140.

BARTZSCH, H., GLÖSS, D., BÖCHER, B., FRACH, P. & GOEDICKE, K. 2003 Properties of SiO2 and Al2O3 films for electrical insulation applications deposited by reactive pulse magnetron sputtering. *Surf. Coat. Technol*. **174–175**, 774–778.

BRÄUER, G., SZYSZKA, B., VERGÖHL, M. & BANDORF, R. 2010 Magnetron sputtering – milestones of 30 years. *Vacuum* **84** (12), 1354–1359, selected Papers from the Proceedings of The Tenth International Symposium on Sputtering and Plasma Processes (ISSP 2009), 8th–10th July 2009, Kanazawa, Japan.

CHABERT, P., PROUST, N., PERRIN, J. & BOSWELL, R.W. 2000 High rate etching of 4H–SiC using a SF6/O2 helicon plasma. *Appl. Phys. Lett*. **76** (16), 2310–2312.

DAVIDSE, P.D. & MAISSEL, L.I. 1966 Dielectric thin films through rf sputtering. *J. Appl. Phys*. **37** (2), 574–579.

DOERNER, R.P., WHYTE, D.G. & GOEBEL, D.M. 2003 Sputtering yield measurements during low energy xenon plasma bombardment. *J. Appl. Phys*. **93** (9), 5816–5823.

GHAILANE, A., MAKHA, M., LARHLIMI, H. & ALAMI, J. 2020 Design of hard coatings deposited by HiPIMS and dcMS. *Mater. Lett*. **280**, 128540.

GRECZYNSKI, G., LU, J., JENSEN, J., BOLZ, S., KÖLKER, W., SCHIFFERS, C., LEMMER, O., GREENE, J. & HULTMAN, L. 2014 A review of metal-ion-flux-controlled growth of metastable tialn by HiPIMS/dcMS co-sputtering. *Surf. Coat. Technol*. **257**, 15–25, 25 years of TiAlN hard coatings in research and industry.

GREENE, J.E. 2017 Tracing the recorded history of thin-film sputter deposition: from the 1800s to 2017. *J. Vac. Sci. Technol.* A **35** (5), 05C204.

GUDMUNDSSON, J.T. 2020 Physics and technology of magnetron sputtering discharges. *Plasma Sour. Sci. Technol*. **29** (11), 113001.

KANNO, I., HAYASHI, S., TAKAYAMA, R. & HIRAO, T. 1996 Superlattices of PbZrO3 and PbTiO3 prepared by multi-ion-beam sputtering. *Appl. Phys. Lett*. **68** (3), 328–330.

MAHNE, N., ČEKADA, M. & PANJAN, M. 2022 Total and differential sputtering yields explored by SRIM simulations. *Coatings* **12** (10), 1541.

MARIKKANNAN, M., SUBRAMANIAN, M., MAYANDI, J., TANEMURA, M., VISHNUKANTHAN, V. & PEARCE, J.M. 2015 Effect of ambient combinations of argon, oxygen, and hydrogen on the properties of dc magnetron sputtered indium tin oxide films. *AIP Adv*. **5** (1), 017128.

MOREL, E., ROZIER, Y., EL FARSY, A. & MINEA, T. 2023 Impact of self-sputtering in high power impulse magnetron sputtering (HiPIMS) with helium. *J. Appl. Phys*. **133** (15), 153301.

MUÑOZ-GARCÍA, J., VÁZQUEZ, L., CASTRO, M., GAGO, R., REDONDO-CUBERO, A., MORENO-BARRADO, A. & CUERNO, R. 2014 Self-organized nanopatterning of silicon surfaces by ion beam sputtering. *Mater. Sci. Engng:* R*: Rep*. **86**, 1–44.

NIHEI, Y., SASAKAWA, Y. & OKIMURA, K. 2008 Advantages of inductively coupled plasma-assisted sputtering for preparation of stoichiometric VO2 films with metal–insulator transition. *Thin Solid Films* **516** (11), 3572–3576.

RIZZO, A., TAGLIENTE, M., CANEVE, L. & SCAGLIONE, S. 2000 The influence of the momentum transfer on the structural and optical properties of znse thin films prepared by r.f. magnetron sputtering. *Thin Solid Films* **368** (1), 8–14.

SARAKINOS, K., ALAMI, J. & KONSTANTINIDIS, S. 2010 High power pulsed magnetron sputtering: a review on scientific and engineering state of the art. *Surf. Coat. Technol*. **204** (11), 1661–1684.

SCHELFHOUT, R., STRIJCKMANS, K. & DEPLA, D. 2020 Sputter yield measurements to evaluate the target state during reactive magnetron sputtering. *Surf. Coat. Technol*. **399**, 126097.

SHIMIZU, S. & TAKAHASHI, K. 2023 Assessment of a thrust induced by a water-fueled magnetron sputtering source. *Acta Astronaut*. **204**, 370–375.

https://doi.org/10.1017/S0022377824000485 Published online by Cambridge University Press

SOMOGYVÁRI, Z., LANGER, G., ERDÉLYI, G. & BALÁZS, L. 2012 Sputtering yields for low-energy Ar+- and Ne+-ion bombardment. *Vacuum* **86** (12), 1979–1982.

TAKAHASHI, K., KOMURO, A. & ANDO, A. 2015 Measurement of plasma momentum exerted on target by a small helicon plasma thruster and comparison with direct thrust measurement. *Rev. Sci. Instrum*. **86** (2), 023505.

TAKAHASHI, K. & MIURA, H. 2021*a* Comparison of thrusts imparted by a magnetron sputtering source operated in DC and high power impulse modes. *AIP Adv*. **11** (10), 105115.

TAKAHASHI, K. & MIURA, H. 2021*b* Direct measurement of thrust induced by a magnetron sputtering source. *Appl. Phys. Lett*. **118** (15), 154101.

TAKAHASHI, K., SAITO, T., ANDO, A., YABUTA, Y., MIZUGUCHI, H., YAMAMOTO, N., KAMEI, R. & HARA, S. 2020 Minimal multi-target plasma sputtering tool. *Vacuum* **171**, 109000.

ZHANG, W., LI, Y., ZHU, S. & WANG, F. 2004 Influence of argon flow rate on TiO2 photocatalyst film deposited by dc reactive magnetron sputtering. *Surf. Coat. Technol*. **182** (2), 192–198.